Supporting Information for

An Underappreciated Aqueous Pathway for Particle Oxidative Potential (OP): Mechanistic Insights into OP-Relevant Products from α-Dicarbonyl and Reduced Nitrogen Reactions

Yulong Pang[1], Fobang Liu[1,*], Yujing Wang[1], Xin Zhang[2], Xu Yang[1], Yanan Wang[1], Chi He[1], Yuemei Han[2,*], Theodora Nah[3]

[1]Department of Environmental Science and Engineering, School of Energy and Power Engineering, Xi'an Jiaotong University, Xi'an 710049, China

[2]Key Laboratory of Aerosol Chemistry and Physics, State Key Laboratory of Loess Science, Institute of Earth Environment, Chinese Academy of Sciences, Xi'an 710061, China

[3]School of Energy and Environment and State Key Laboratory of Marine Environmental Health, City University of Hong Kong, Hong Kong SAR 999077, China

[*]Corresponding author: Fobang Liu (fobang.liu@xjtu.edu.cn); Yuemei Han (yuemei.han@ieecas.cn)

Number of Pages: 30

Number of Texts: 2

Number of Figures: 20

Number of Tables: 4

Text S1 Methods in the quantification of oxidative potential

Measurement of OP^{DTT}: In the DTT depletion assay, a 2 mL reaction solution was prepared by combining 200 μL of the sample with 100 μM DTT in PBS and incubating the mixture at 37 °C for 30 min. During the incubation, 200 μL aliquots of the mixture were withdrawn at 5 min intervals and reacted with 10 μL of DTNB (0.24 mM) and 100 μL of tris buffer (6.45 mM containing 20 mM EDTA). The absorbance at 412 nm was measured using a SuPerMax 3000FA microplate reader (Shanghai Flash Spectrum). To quantify the net DTT consumption, the background absorbance from the sample and reaction matrix was subtracted from the measured values. All procedures were conducted under dark conditions to minimize potential light interference.

OP^{DTT} was determined from the residual DTT concentration measured at various time points. This value was derived from the slope and intercept of a linear regression model fitted to the absorbance-time data (Fang et al., 2015). Due to the high background absorbance of reaction products, which may interfere with accurate DTT depletion detection, samples were appropriately diluted to minimize matrix effects. Specifically, dilution factors (20-40x dilutions) were selected to ensure that the background absorbance of the reaction mixtures remained below the minimum absorbance observed during DTT depletion measurements. To validate the linearity assumption of this approach, a series of dilution factors was tested under representative conditions (MG+Gly, pH 7, 48 h; Figure S20a). The resulting OP^{DTT} values were consistent across dilutions, with a relative standard deviation of 2.05%. The obtained OP^{DTT} values from diluted samples were subsequently corrected by the corresponding dilution factors to enable comparison across different conditions.

Measurement of OP^{OH}: In the •OH production assay, •OH generation was quantified using a fluorescence-based method. Briefly, 200 μL of the sample was mixed with 200 μL of 10 mM TPT (200 μl) and 80 μL of 200 μM ascorbic acid in PBS and incubated at 37°C for 60 min. During the incubation, TPT reacted with the generated •OH to form the stable and strongly fluorescent product 2-hydroxyterephthalic acid (2-OHTA). At specified time intervals (10, 20, 30, 40, 50, 60 min),

200 μL aliquots were withdrawn and immediately mixed with 100 μL of DMSO (100 mM in PBS) to quench further •OH formation (Son et al., 2015). Fluorescence of 2-OHTA was measured at an excitation/emission wavelength of 310/425 nm using a microplate reader (SuPerMax 3000FA, Shanghai Flash Spectrum).

The net •OH generation rate was determined by subtracting the possible fluorescence from the sample and matrix from the measured signal. The •OH generation rate was calculated based on the determined 2-OHTA concentration at different time intervals, as the formation of 2-OHTA is proportional to the generation of •OH. Quantification of 2-OHTA was performed using daily calibration curves prepared from 2-OHTA standard (TCI) at concentrations of 0, 2, 3, 4, 5, and 6 μM. The •OH concentration was calculated by the following equation:

$$(\cdot OH) = \frac{(2-OHTA)}{y_{2-OHTA}}$$

where (*2-OHTA*) is the measured concentration of 2-OHTA, $y_{2\text{-}OHTA}$ is the molar yield of 2-OHTA from the reaction of •OH with TPT in PBS, which is 0.35 at pH 7.2 (Li et al., 2018). To avoid potential interference from the fluorescence of the products, samples were diluted (200-400x dilutions) to ensure the background absorbance was lower than the minimum fluorescence signal associated with •OH formation. Similar to the DTT assay, a series of dilution tests confirmed a linear response of •OH formation within the applied dilution range (Figure S20b). Consistent OPOH values were obtained across dilutions, with a relative standard deviation of 2.46%. The resulting •OH production values were corrected by the corresponding dilution factors.

Text S2 UHPLC-HRMS/MS data processing

UHPLC–HRMS/MS data were processed using the open-source software MZmine 2 (http://mzmine.github.io/) for peak deconvolution and chromatogram construction. Structural elucidation of reaction products was performed using SIRIUS 5.0, a tool designed for small molecule identification, which interprets molecular structures via MS/MS fragmentation tree analysis. Molecular formulas were assigned with a mass tolerance of ±2 ppm. SIRIUS has been shown to perform well in predicting molecular structures within complex atmospheric organic aerosol matrices (Yang et al., 2023).

For the identified molecular species, the modified aromaticity index (AImod) was calculated. Based on the assigned

63 molecular formula ($C_nH_hN_nO_oS_s$), AImod can be calculated as:

64 $$AI_{mod} = \frac{1 + c - 0.5o - s - 0.5h}{c - 0.5o - s - n}$$

65 where *c, h, n, o*, and s denote the numbers of carbon, hydrogen, nitrogen, oxygen, and sulfur atoms, respectively. The
66 intensity-weighted average elemental composition (C, H, O, N) and AImod for each sample was calculated using the
67 following equations:

68 $$(M)_w = \left(\sum_i I_i \times (M)_i\right) / \sum_i I_i$$

69 where *M* represents either an elemental composition (C, H, O, N) or AImod. The subscript w indicates an intensity-weighted
70 average, *Ii* is the relative abundance of mass spectral peak i, and *(M)i* represents the corresponding value of M for that
71 peak.
72

Table S1. NMR signals monitored for reactant and product species.

^{1}H chemical environment	Functional group	NMR chemical shift (ppm)
aliphatic hydrogen	H-C	0.6-1.8
unsaturated alkyl hydrogen	H-C-C=	1.8-3.2
oxygenated aliphatic hydrogen	H-C-O	3.2-4.4
aromatic hydrogen	Ar-H	6.0-9.0

Table S2. The OP^{DTT} (μM/min) of the four reaction systems under different conditions.

Time	MG+Gly				MG+AS				GX+Gly				GX+AS			
	pH7	ph6	pH5	pH3	pH7	ph6	pH5	pH3	pH7	ph6	pH5	pH3	pH7	ph6	pH5	pH3
4h	36.13 ± 5.14	1.99 ± 0.05	0.38 ± 0.01	0.11 ± 0.01	0.20 ± 0.01	0.24 ± 0.02	0.21 ± 0.02	0.23 ± 0.02	1.57 ± 0.01	0.59 ± 0.12	0.44 ± 0.08	0.25 ± 0.11	0.09 ± 0.01	0.07 ± 0.01	0.15 ± 0.02	0.25 ± 0.15
24h	59.77 ± 3.00	15.94 ± 0.75	1.73 ± 0.11	0.19 ± 0.01	0.45 ± 0.00	0.38 ± 0.02	0.35 ± 0.02	0.25 ± 0.02	0.82 ± 0.06	0.76 ± 0.08	0.49 ± 0.11	0.33 ± 0.01	0.13 ± 0.01	0.15 ± 0.003	0.16 ± 0.05	0.35 ± 0.04
48h	90.24 ± 8.61	40.2 ± 6.14	7.34 ± 1.14	0.78 ± 0.06	0.91 ± 0.04	0.95 ± 0.06	0.4 ± 0.02	0.22 ± 0.01	1.02 ± 0.07	1.02 ± 0.1	0.53 ± 0.01	0.3 ± 0.02	0.17 ± 0.01	0.15 ± 0.02	0.18 ± 0.01	0.38 ± 0.02
96h	122.4 ± 2.43	105.6 ± 4.32	18.31 ± 0.48	1.31 ± 0.13	1.34 ± 0.07	1.34 ± 0.1	0.36 ± 0.01	0.19 ± 0.02	0.87 ± 0.05	0.95 ± 0.05	0.5 ± 0.09	0.37 ± 0.04	0.35 ± 0.03	0.23 ± 0.05	0.21 ± 0.07	0.27 ± 0.10
144h	127.4 ± 13.87	192.0 ± 11.63	45.16 ± 0.26	2.48 ± 0.16	1.91 ± 0.11	1.51 ± 0.17	0.42 ± 0.03	0.43 ± 0.02	1.04 ± 0.35	0.69 ± 0.07	0.31 ± 0.11	0.25 ± 0.14	0.18 ± 0.02	0.13 ± 0.01	0.09 ± 0.001	0.2 ± 0.08

Table S3. The OP^{OH} (μM×10^{-2}/min) of the four reaction systems under different conditions.

Time	MG+Gly				MG+AS				GX+Gly				GX+AS			
	pH7	ph6	pH5	pH3	pH7	ph6	pH5	pH3	pH7	ph6	pH5	pH3	pH7	ph6	pH5	pH3
4h	227.1 ± 22.22	85.14 ± 2.42	62.86 ± 3.23	1.69 ± 0	0.73 ± 0.02	1.01 ± 0.02	1.41 ± 0.10	1.17 ± 0.04	0.77 ± 0.16	0.97 ± 0.24	1.06 ± 0.20	0.91 ± 0.20	0.00 ± 0.00	53.14 ± 6.06	2.77 ± 0.24	4.86 ± 1.21
24h	560 ± 8.08	247.1 ± 10.1	94.76 ± 7.41	1.24 ± 0.14	35.14 ± 2.02	23.43 ± 0.27	1.13 ± 0.02	0.94 ± 0.08	35.57 ± 8.28	38.4 ± 3.07	42.06 ± 10.34	7.46 ± 1.11	86.43 ± 7.07	56.43 ± 3.31	52.57 ± 6.46	11.79 ± 1.31
48h	1034 ± 56.6	557.1 ± 36.4	315.7 ± 22.2	2.23 ± 0.24	60.95 ± 5.39	36.57 ± 4.85	1.89 ± 0.08	0.83 ± 0.00	54.0 ± 4.44	42.86 ± 12.1	57.71 ± 10.5	9.50 ± 0.91	129.7 ± 18.6	108.6 ± 8.08	71.71 ± 12.5	12.79 ± 2.12
96h	1086 ± 16.2	511.4 ± 28.3	318.6 ± 10.1	1.37 ± 0.08	77.14 ± 8.08	90.57 ± 5.25	2.09 ± 0.04	0.93 ± 0.06	89.14 ± 11.31	89.14 ± 11.3	120.0 ± 25.3	17.14 ± 4.04	345.7 ± 8.08	211.4 ± 24.24	129.1 ± 16.2	22.29 ± 2.02
144h	834.3 ± 32.3	468.6 ± 24.2	300 ± 12.1	1.77 ± 0.08	62.38 ± 2.02	97.71 ± 1.62	1.46 ± 0.04	0.87 ± 0.02	106.9 ± 0.81	80.00 ± 16.2	116.0 ± 28.4	19.71 ± 1.21	317.1 ± 8 .08	234.3 ± 32.32	120.6 ± 2.42	27.29 ± 1.41

Table S4. A summary of the observed OP^{OH} trends, key molecular species identified by MS, structural features revealed by NMR, and the proposed mechanistic links to OP activity for each reaction system.

Reaction system	OP^{OH} trend	Key molecular species	Structural features	Proposed mechanism to •OH generation
MG+Gly	Highest activity: consistently highest OP^{OH}. pH-dependent: Increase with pH. Kinetics: rapid rise in first 48h, then plateau.	Side chains: >35% adjacent to unprotonated N-bases contain carboxyl groups. Other products: high abundance of CHO species.	Aromatic protons (Ar-H) relatively low compared to GX+AS,reflecting dominance of functional groups (e.g., carboxylates) over polycyclic structures.	Electronic effect: electron-withdrawing carboxyl groups enhance electron-transfer capability of unprotonated N-base, driving highly efficient •OH generation.
GX+AS	High activity: second highest OP^{OH}. pH-dependent: increase with pH. Kinetics: delayed rise between 48 and 96 h.	Side chains: mainly carbonyl and hydroxyl groups. Aromaticity: high (~1.74-1.75); dominated by polycyclic N-heterocycles (>2 rings).	High proportion of Ar-H compared to other systems.	Conjugation effect: polycyclic aromatic structures with extended conjugation strengthen electron-transfer capability of unprotonated N-bases, promoting substantial •OH formation.
GX+Gly	Lower activity: lower OP^{OH}. pH-independent: comparable values across pH 5–7 . Kinetics: Delayed rise between 48 and 96 h.	Carboxylated side chains present, but low abundance of unprotonated N-base species. Signal intensities comparable at pH 5 and 7.	Concentrations of Ar-H remain comparable across pH 5-7.	Abundance limitation: Although carboxyl groups enhance electron transfer, low abundance of reactive species limits total •OH. Comparable Ar-H explains pH-independent OP^{OH}.

Reaction system	OP^{OH} trend	Key molecular species	Structural features	Proposed mechanism to •OH generation
MG+AS	<u>Lowest activity:</u> Consistently lowest OP^{OH}. <u>pH-independent:</u> Comparable at pH 6–7 . <u>Kinetics:</u> rapid initial rise but extremely low absolute values.	<u>Side chains:</u> >70% of side chains adjacent to unprotonated N-bases are methyl groups. <u>Aromaticity:</u> Low aromaticity (<0.67), indicating limited conjugation.	Weak Ar-H signals across all conditions.	<u>Suppression effect:</u> Electron-donating methyl groups increase N-heterocycle electron density, reducing electron-transfer capacity. Low aromaticity further suppresses •OH formation.

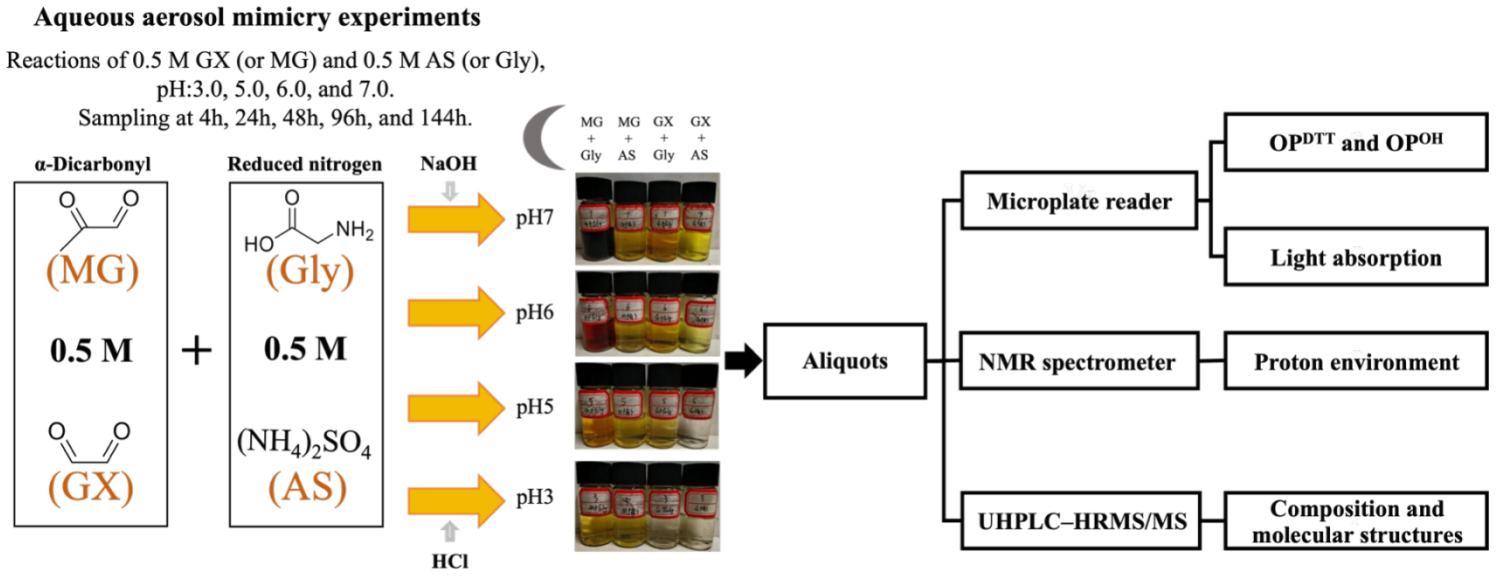

Figure S1. Schematic diagram of the experimental configuration.

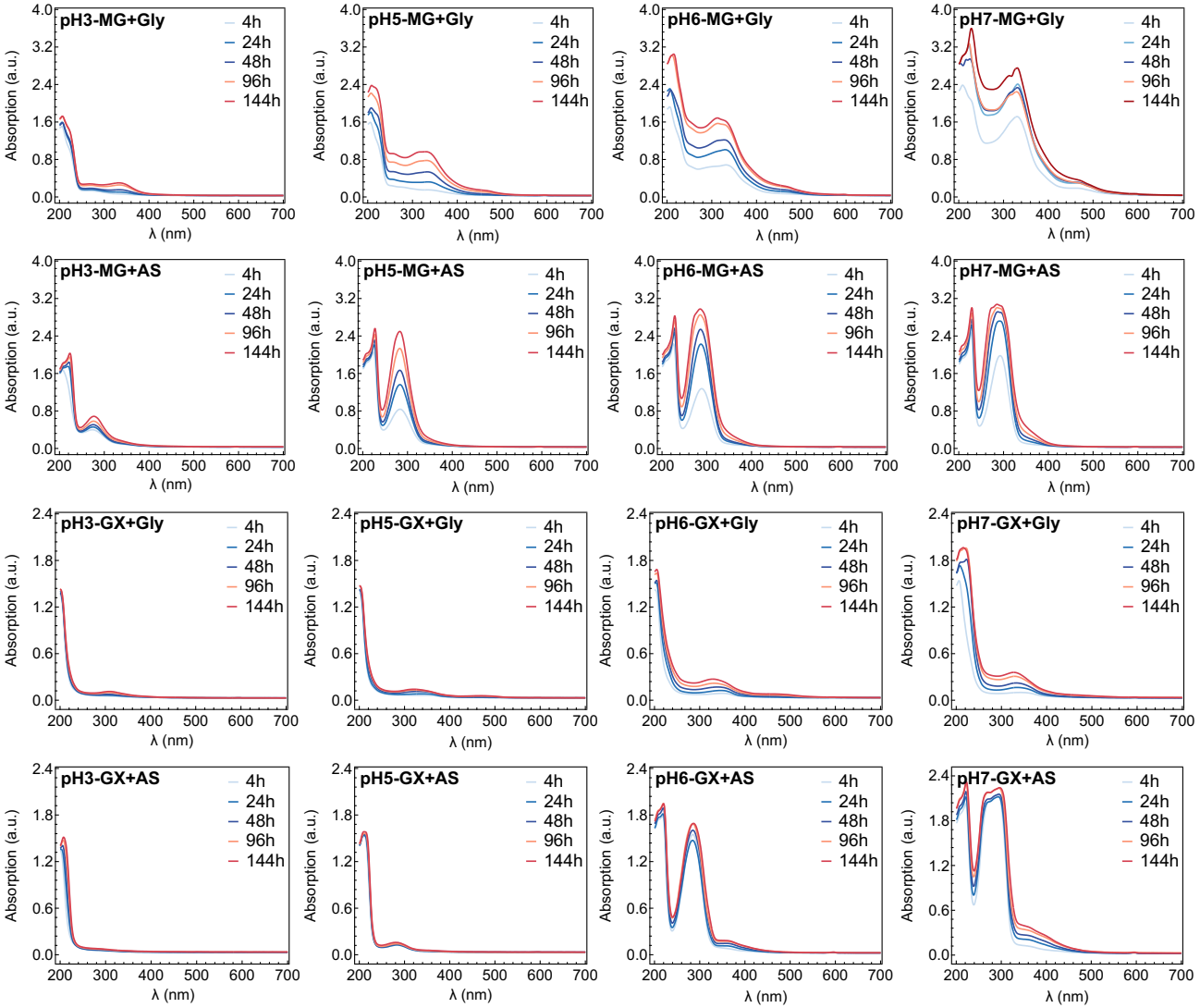

Figure S2. The absorbance (200–700 nm) of the four reaction systems after different reaction times under varying pH conditions.

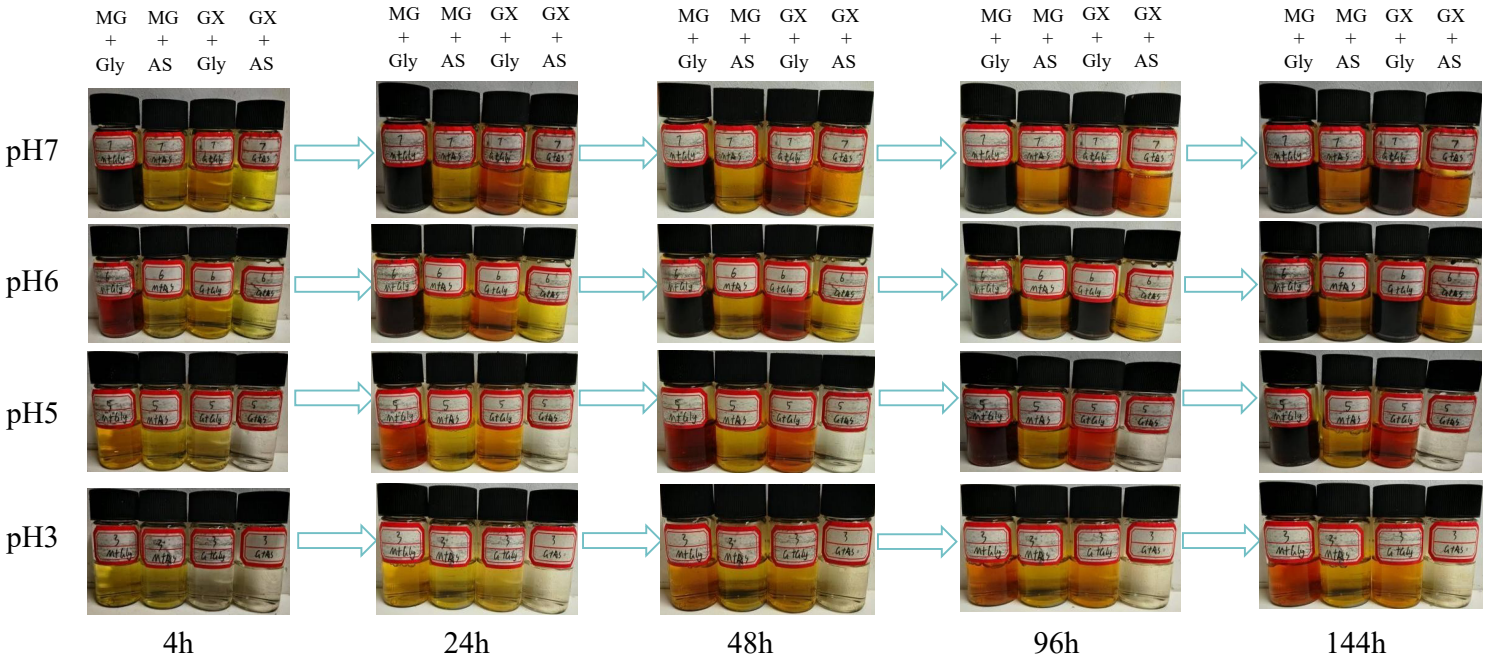

Figure S3. Color changes of the four reaction systems after different reaction times under varying pH conditions.

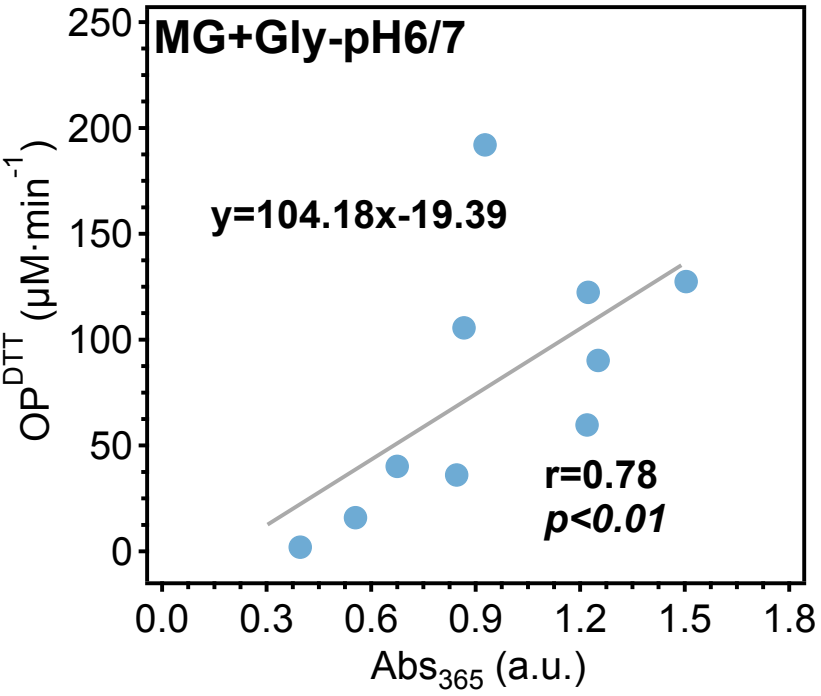

Figure S4. Scatterplots of OP^{DTT} with the BrC absorption coefficient (Abs_{365}) for the MG+Gly system under pH 6–7 conditions. The Spearman correlation coefficients (r) and associated p values are illustrated in the figure. The lines represent linear regressions.

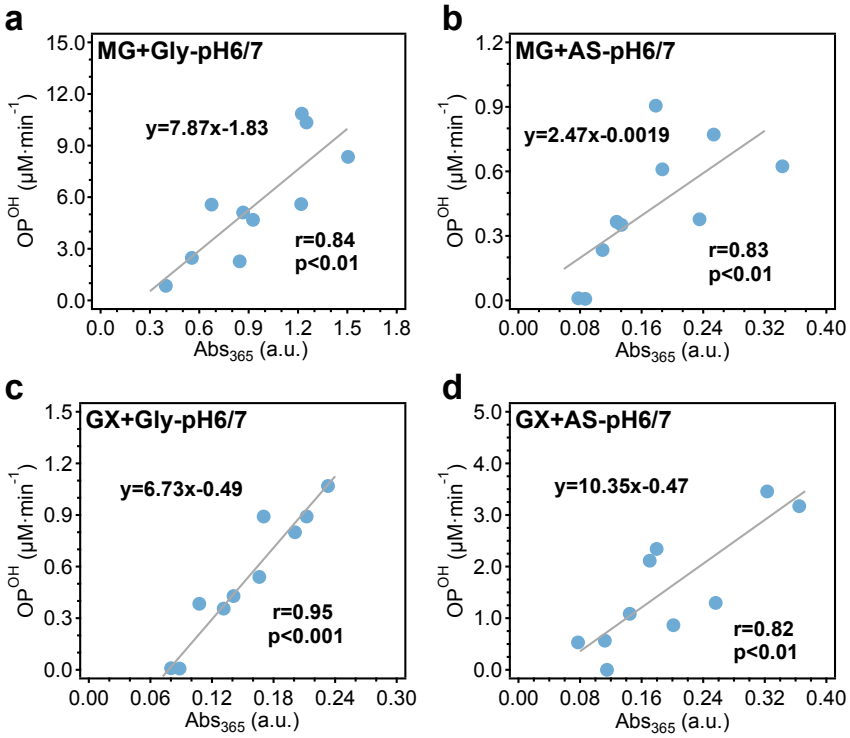

Figure S5. Scatterplots of OP^{OH} with the BrC absorption coefficient (Abs_{365}) for the four reaction systems under pH 6–7 conditions. The Spearman correlation coefficients (r) and associated p-values are illustrated in the figure. The lines represent linear regressions.

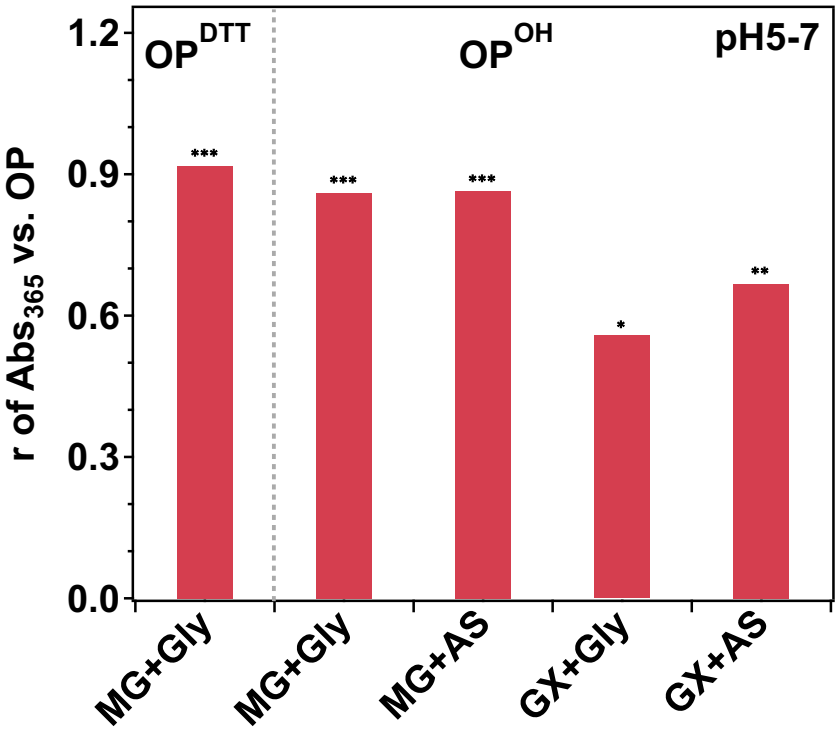

Figure S6. Spearman correlation (represented by the Spearman correlation coefficient, r) between the BrC absorption coefficient (Abs_{365}) and OP metrics (OP^{DTT} for the MG+Gly system; OP^{OH} for all four reaction systems) under pH 5–7 conditions. Statistically significant differences were determined with a t-test using a 95% confidence interval (*, **, and *** indicate $p < 0.05$, $p < 0.01$, and $p < 0.001$, respectively).

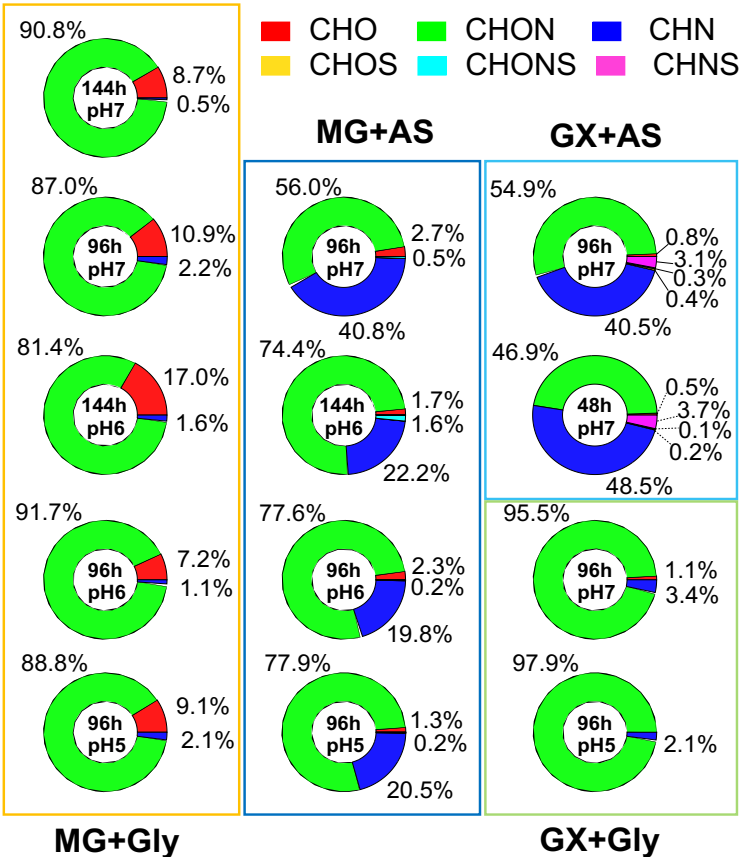

Figure S7. The peak area-weighted fraction of molecular composition for the four reaction systems under different reaction conditions.

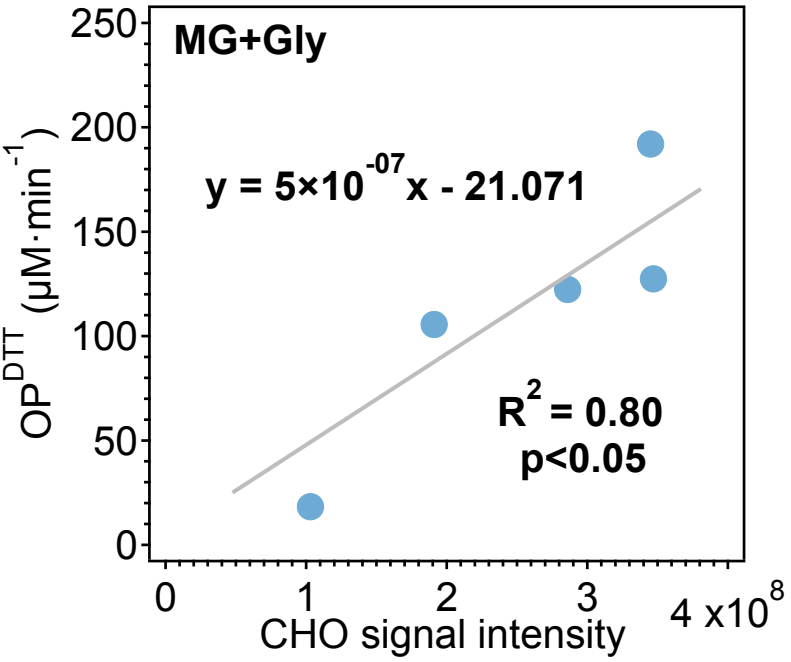

Figure S8. Correlation analysis between OP^{DTT} and the abundance of CHO species in the MG+Gly system.

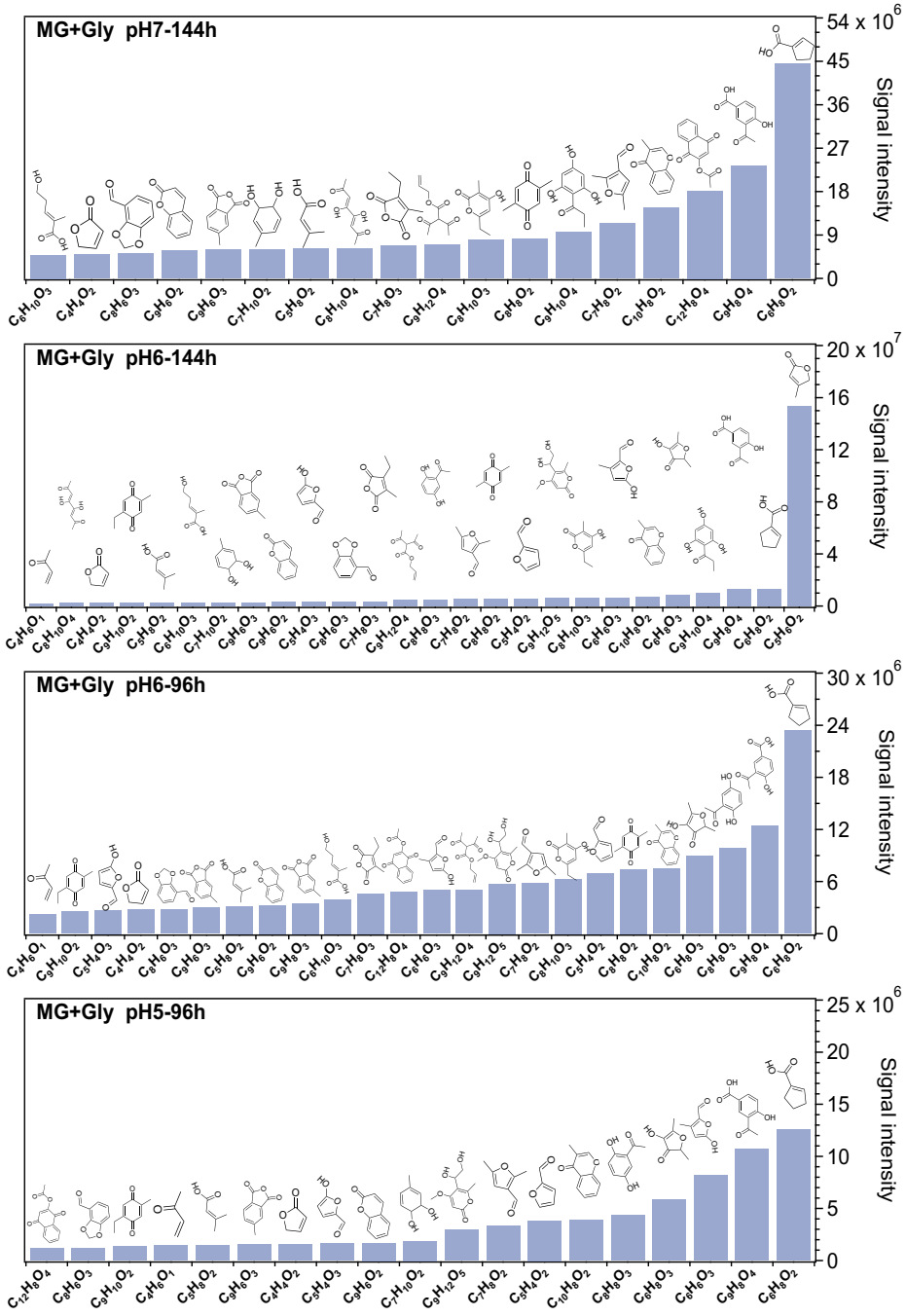

Figure S9. The possible molecular structures of the major CHO species detected in the MG+Gly system under different reaction conditions.

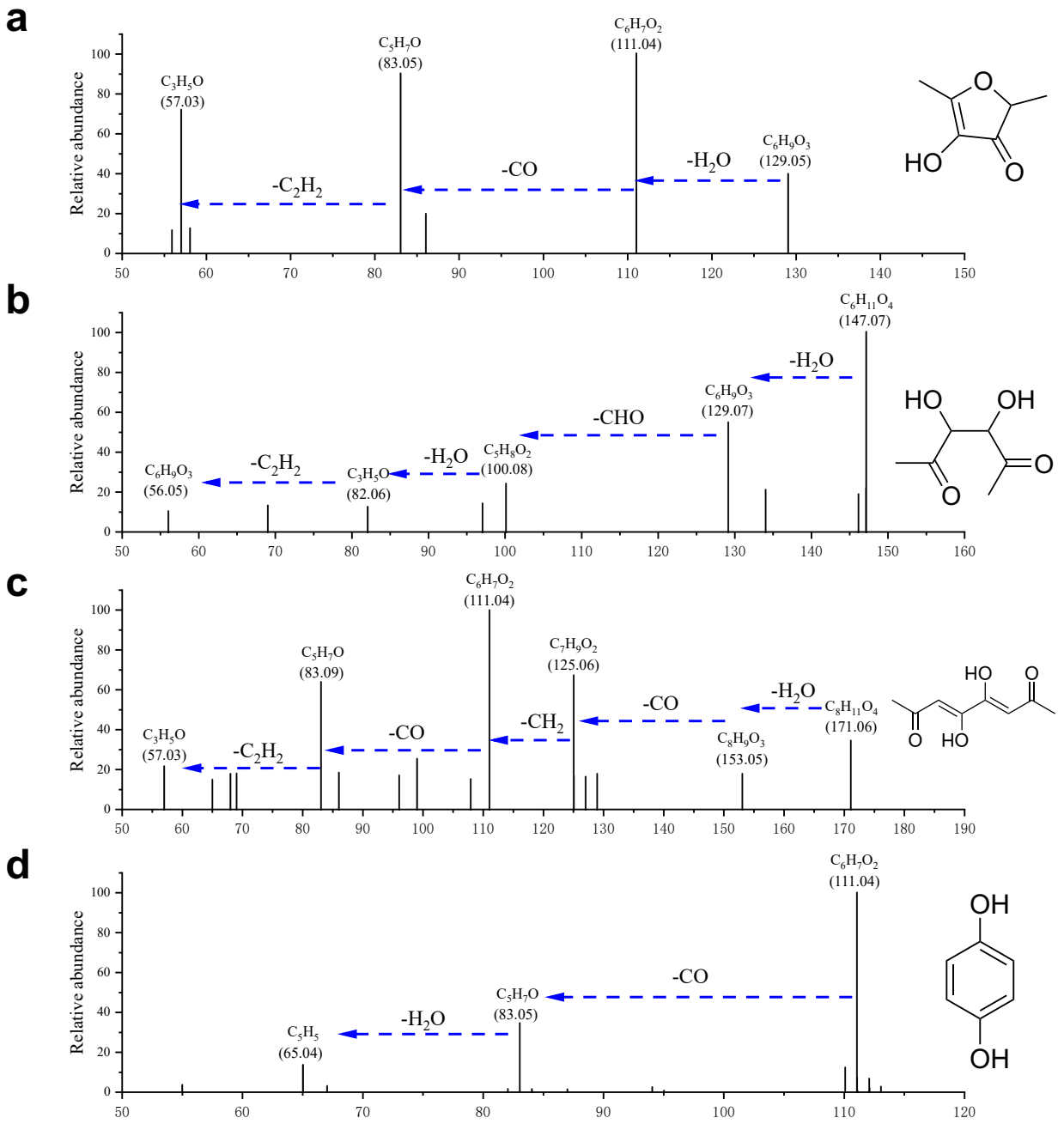

Figure S10. Representative conjugated carbonyl and quinone compounds within CHO species identified in the MG+Gly system based on the MS/MS fragmentation patterns. (a) 2,5-dimethyl-4-hydroxy-3(2H)-furanone ($C_6H_8O_3$), pH6-144h; (b) 3,4-dihydroxy-2,5-hexanedione ($C_6H_{10}O_4$), pH6-144h; (c) 4,5-dihydroxy-3,5-octadiene-2,7-dione ($C_8H_{10}O_4$), pH6-144h. (d) hydroquinone ($C_6H_6O_2$), pH7-96h.

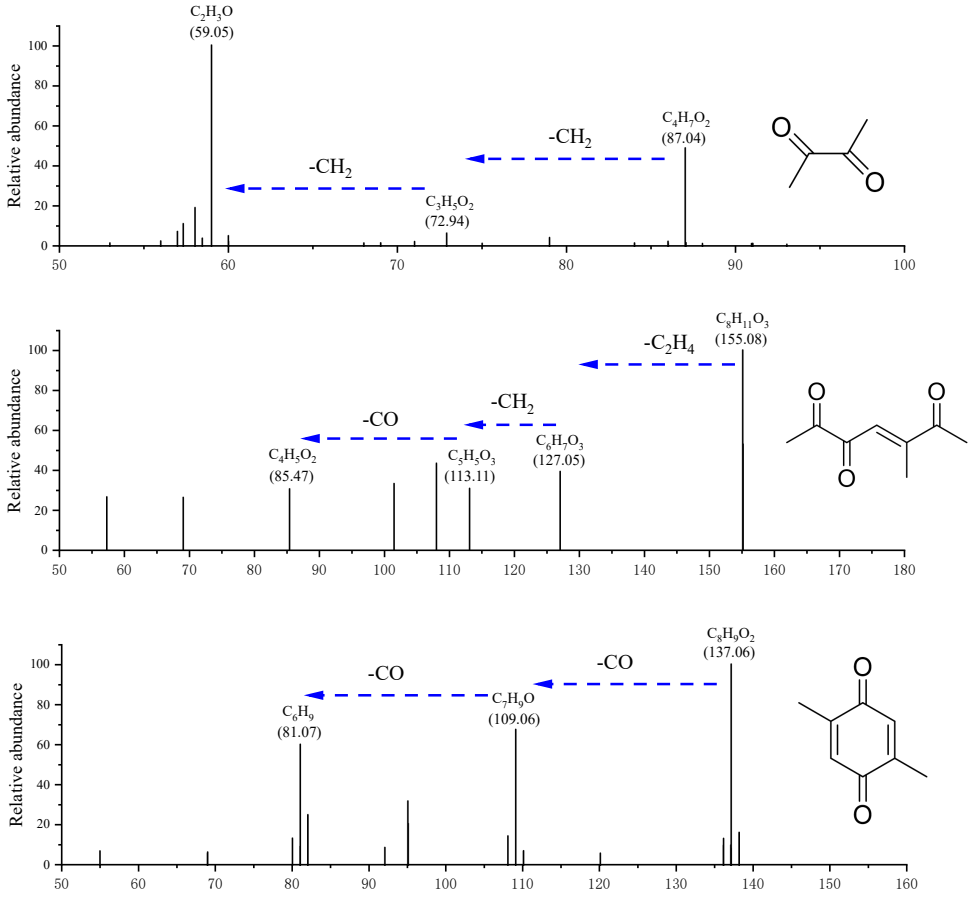

Figure S11. Identification of key intermediates for the formation of 2,5-dimethyl-p-benzoquinone based on the MS/MS fragmentation patterns in the MG+Gly system (pH 7, 144 h; pH 6,96 h; pH 6,144 h).

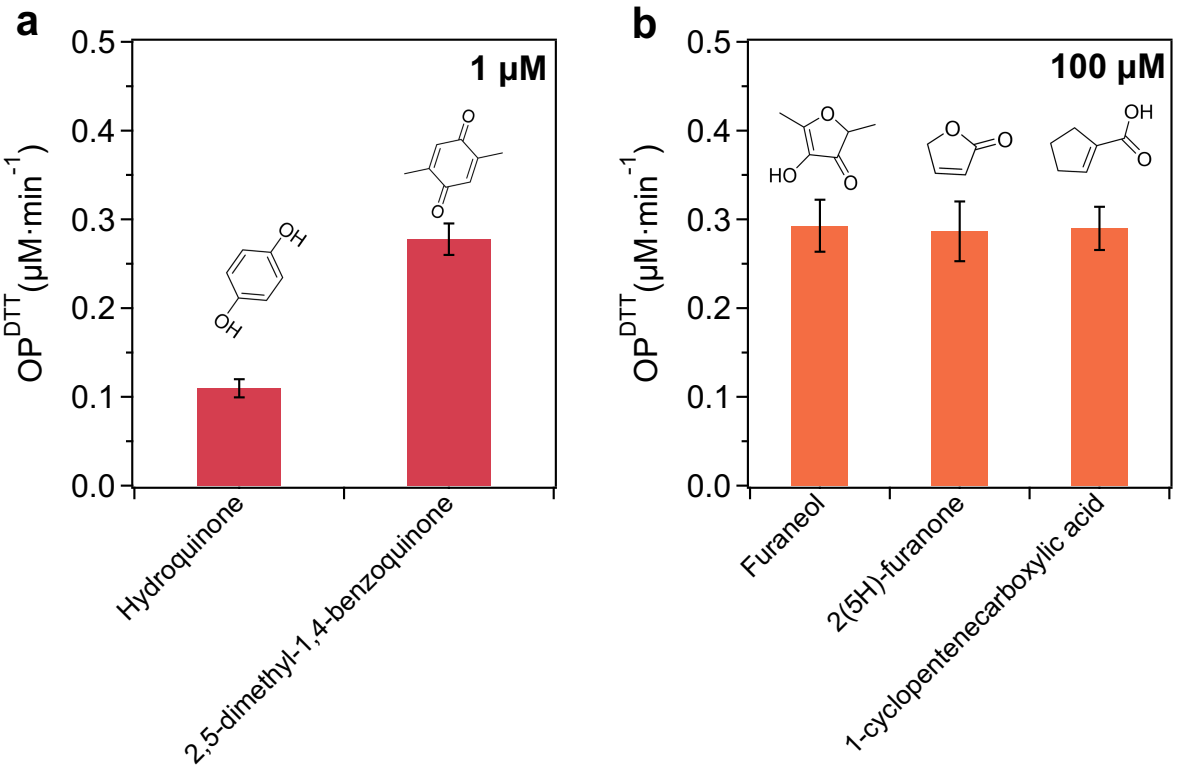

Figure S12. The measured OP^{DTT} for representative CHO compounds. (a) OP^{DTT} of 1 μM hydroquinone and 2,5-dimethyl-1,4-benzoquinone; (b) OP^{DTT} of 100 μM furaneol, 2(5H)-furanone, and 1-cyclopentenecarboxylic acid.

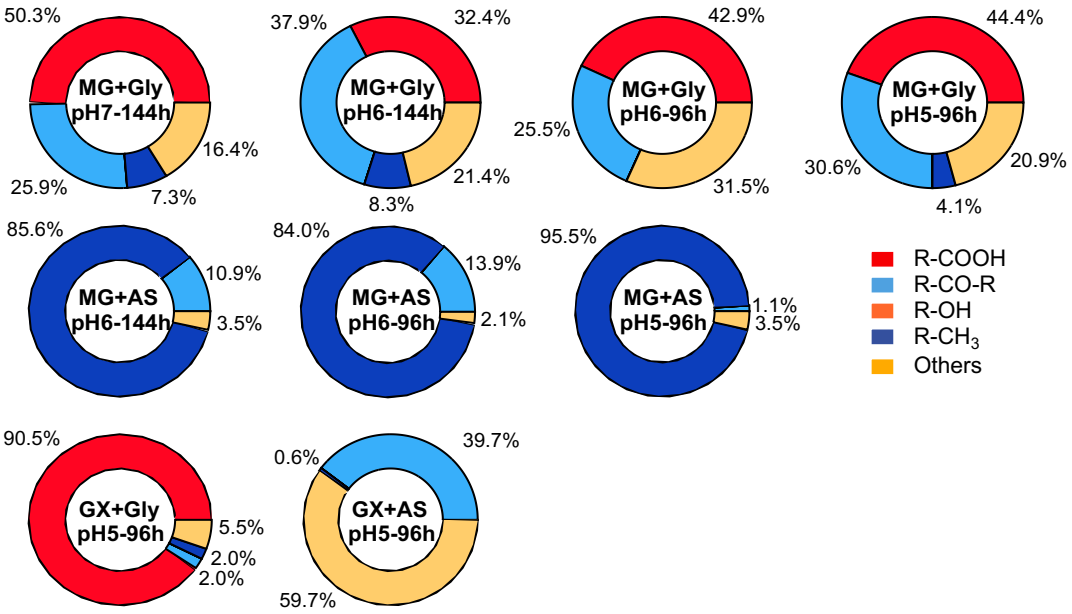

Figure S13. The peak area-weighted proportion of N-heterocycles with different side chains in the four reaction systems under different reaction conditions.

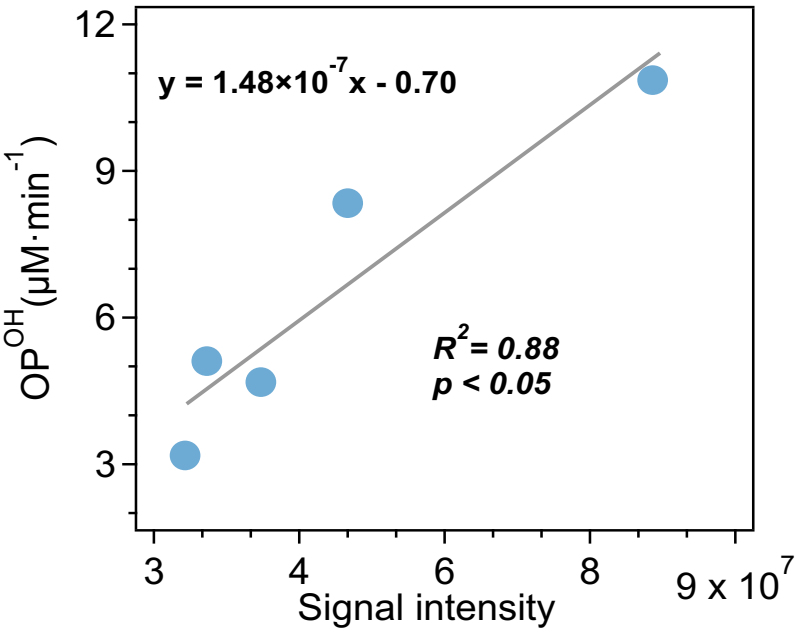

Figure S14. Correlation analysis between OP^{OH} and the signal intensity of N-heterocycles with adjacent carboxyl groups in the MG+Gly system.

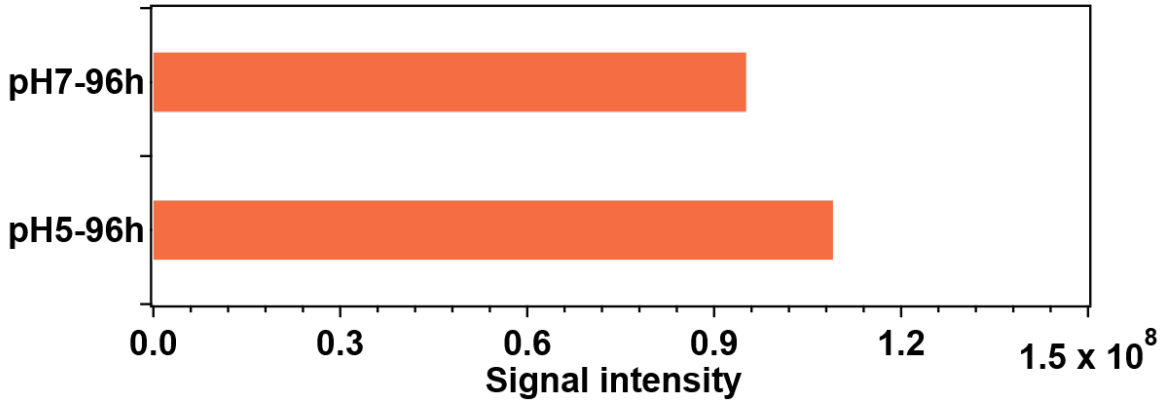

Figure S15. Comparison of signal intensities of unprotonated N-base species in the GX+Gly system at pH 5 and 7 after 96 h of reaction, determined by UHPLC-HRMS/MS.

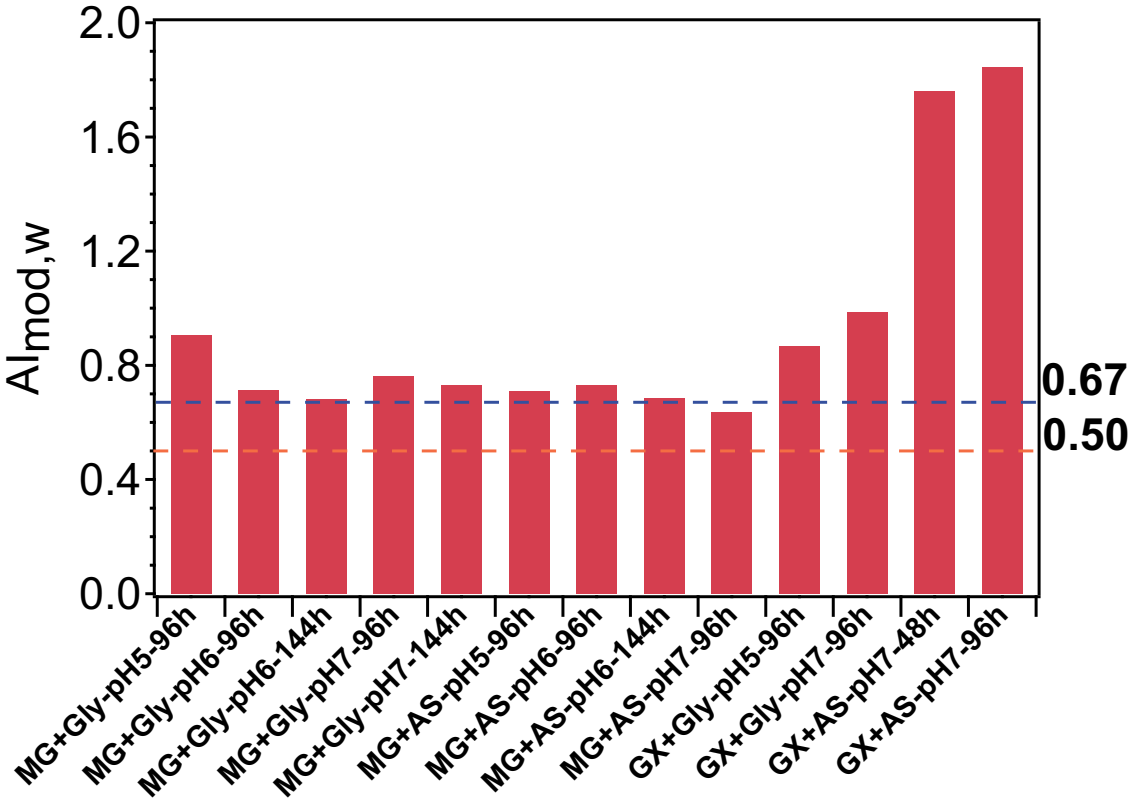

Figure S16. The calculated $AI_{mod,w}$ of N-heterocycles with unprotonated N-base for the four reaction systems under different reaction conditions. The identified compounds can be classified into four categories based on the AI_{mod} values: condensate aromatic ($AI_{mod} \geq 0.67$), aromatic ($0.5 \leq AI_{mod} < 0.67$), olefinic ($0 < AI_{mod} < 0.5$), and aliphatic ($AI = 0$) compounds.

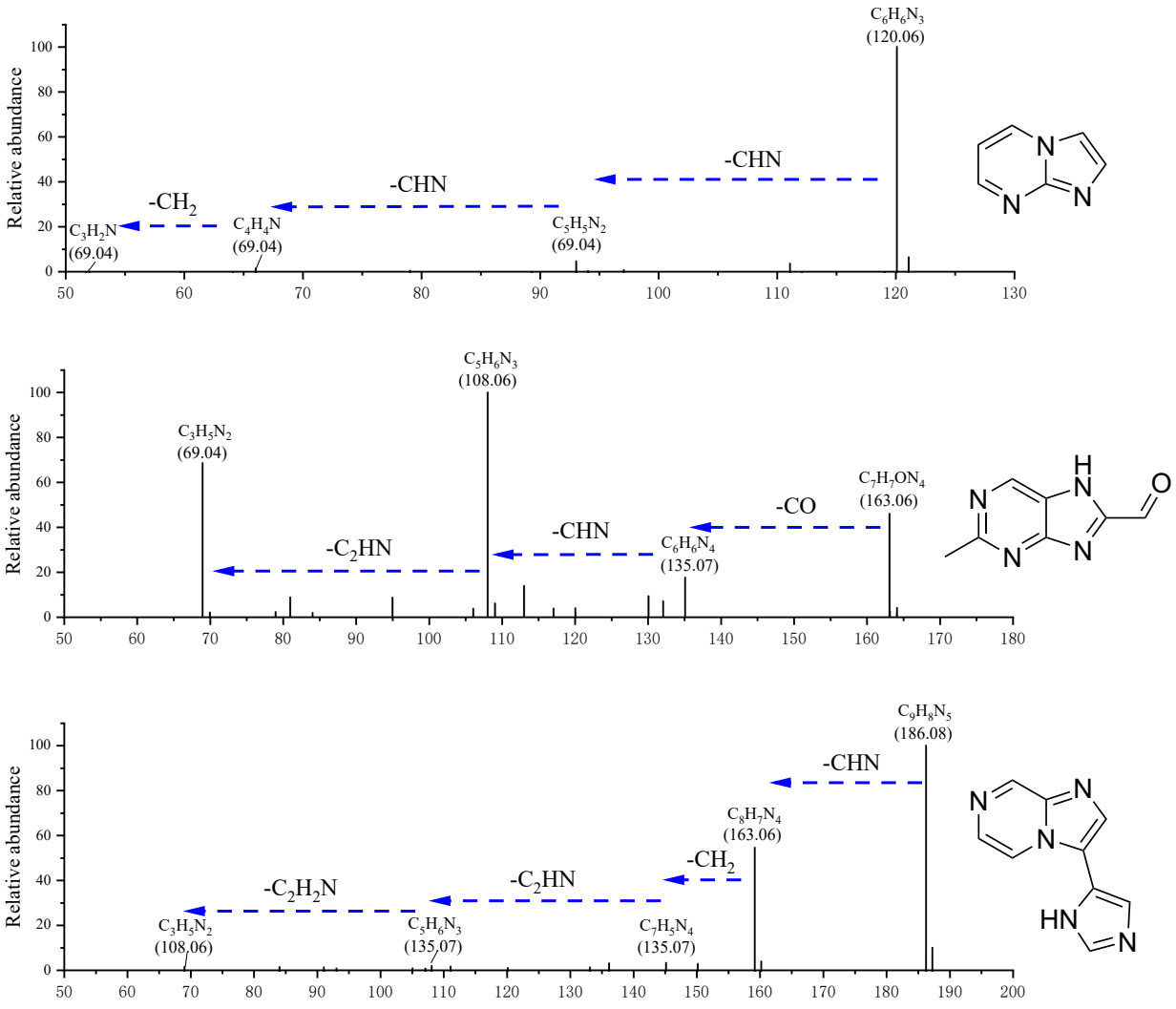

Figure S17. Representative products identified based on the MS/MS fragmentation pattern in the GX + AS system.

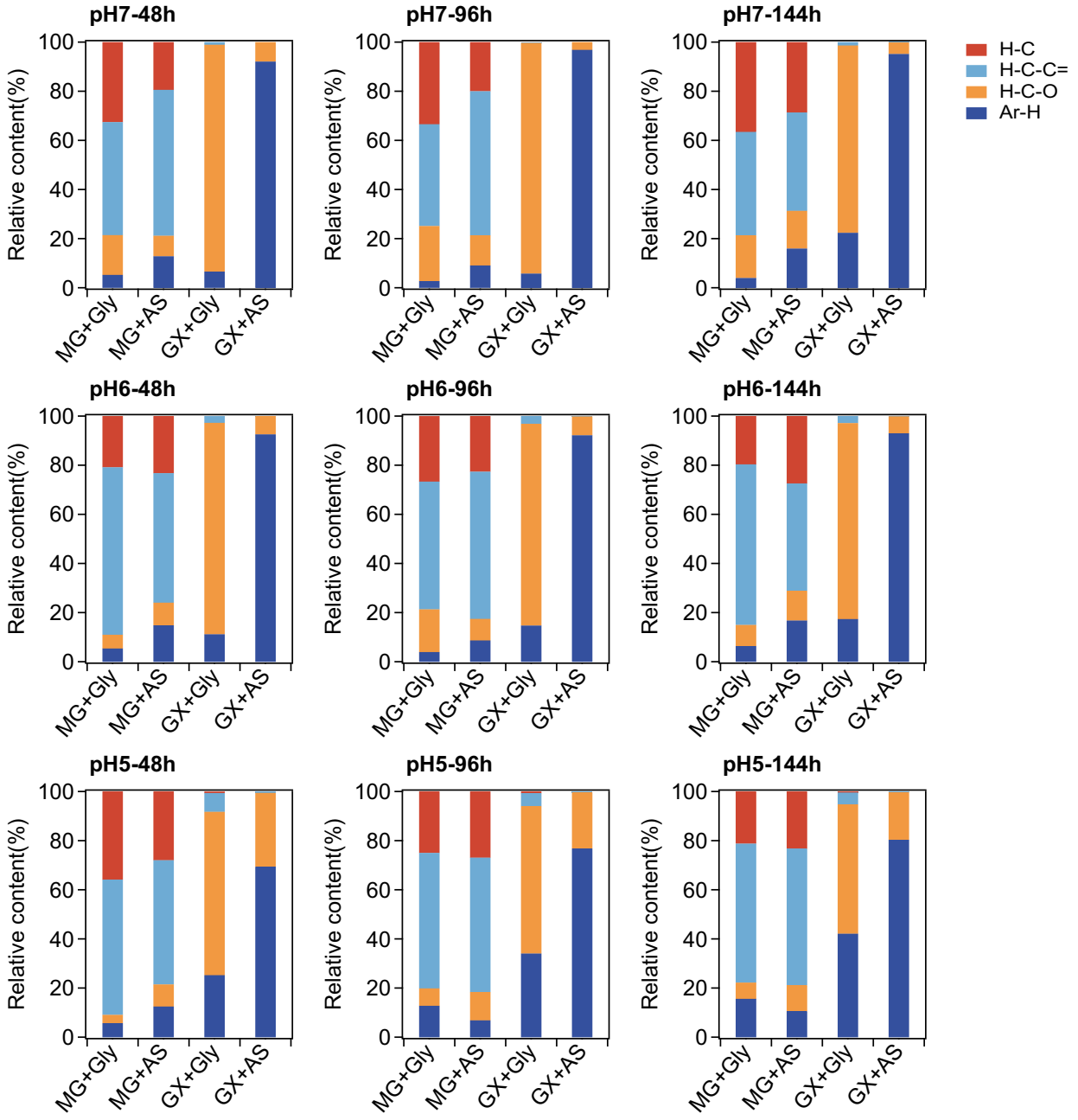

Figure S18. The relative contents of site-specific hydrogen atoms in the four reaction systems under different reaction conditions, as determined by NMR spectroscopy.

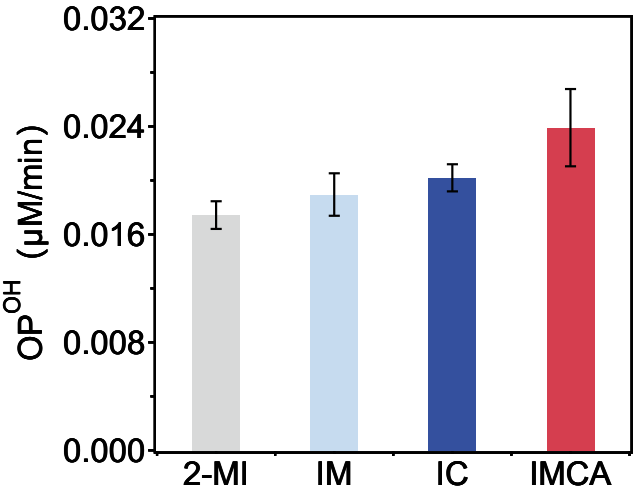

Figure S19. OP^{OH} of typical model compounds of N-heterocycles with an unprotonated N-base. IM: imidazole; 2-MI: 2-methylimidazole; IC: imidazole-2-carboxaldehyde; IMCA: 1H-imidazole-2-carboxylic acid.

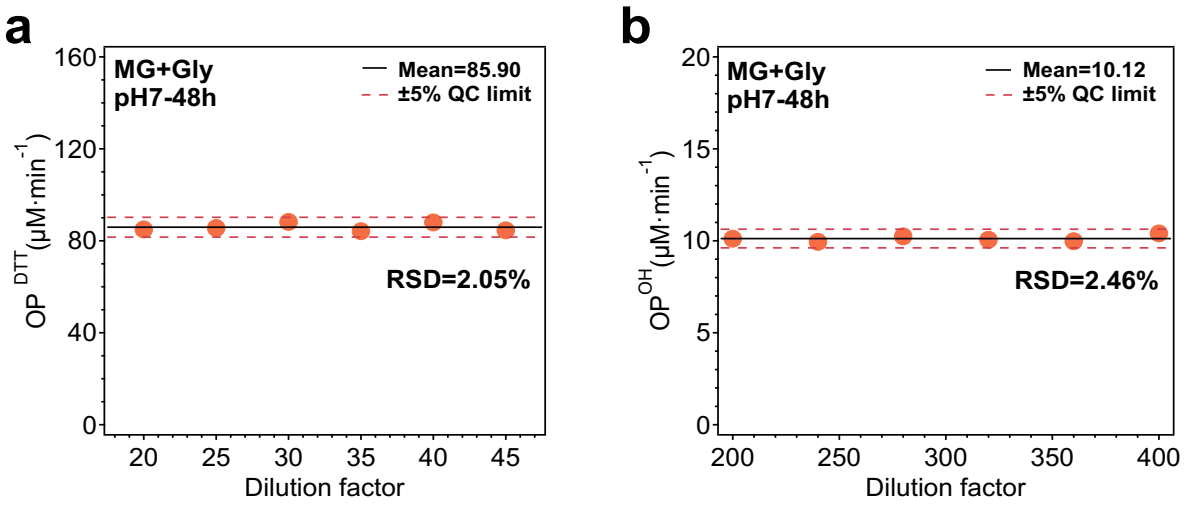

Figure S20. The determined OP^{DTT} (a) and OP^{OH} (b) values with different dilution factors for the MG+Gly system (pH 7, 48 h). The solid black lines represent the dilution-corrected mean OP values, and the red dashed lines indicate the ±5% quality control limits.

References

Fang, T., Verma, V., Guo, H., King, L. E., Edgerton, E. S., and Weber, R. J.: A semi-automated system for quantifying the oxidative potential of ambient particles in aqueous extracts using the dithiothreitol (DTT) assay: results from the Southeastern Center for Air Pollution and Epidemiology (SCAPE), Atmospheric Measurement Techniques, 8, 471-482 http://doi.org/10.5194/amt-8-471-2015, 2015.

Li, X., Kuang, X. M., Yan, C., Ma, S., Paulson, S. E., Zhu, T., Zhang, Y., and Zheng, M.: Oxidative Potential by PM2.5 in the North China Plain: Generation of Hydroxyl Radical, Environmental Science & Technology, 53, 512-520 http://doi.org/10.1021/acs.est.8b05253, 2018.

Son, Y., Mishin, V., Welsh, W., Lu, S.-E., Laskin, J., Kipen, H., and Meng, Q.: A Novel High-Throughput Approach to Measure Hydroxyl Radicals Induced by Airborne Particulate Matter, International Journal of Environmental Research and Public Health, 12, 13678-13695 http://doi.org/10.3390/ijerph121113678, 2015.

Yang, L., Huang, R.-J., Shen, J., Wang, T., Gong, Y., Yuan, W., Liu, Y., Huang, H., You, Q., Huang, D. D., and Huang, C.: New Insights into the Brown Carbon Chromophores and Formation Pathways for Aqueous Reactions of α-Dicarbonyls with Amines and Ammonium, Environmental Science & Technology, 57, 12351-12361 http://doi.org/10.1021/acs.est.3c04133, 2023.